**Proceedings of the 33rd International Conference on Ocean, Offshore and Arctic Engineering**
**OMAE 2014**
**June 8-13, 2014, San Francisco, USA**

**OMAE 2014-24132**

# RESULTS FROM NUMERICAL SIMULATION AND FIELD TESTS OF AN OCEANOGRAPHIC BUOY POWERED BY SEA WAVES

**J.A. Hamilton**
Monterey Bay Aquarium Research Institute
Moss Landing, California, USA

**J.C.C. Henriques**
IDMEC, Instituto Superior Técnico,
Universidade de Lisboa, Portugal

**F. Cazenave**
Monterey Bay Aquarium Research Institute
Moss Landing, California, USA

**P. McGill**
Monterey Bay Aquarium Research Institute
Moss Landing, California, USA

**W. Radochonski**
Monterey Bay Aquarium Research Institute
Moss Landing, California, USA

**A.F.O. Falcão**
IDMEC, Instituto Superior Técnico,
Universidade de Lisboa, Portugal

**L.M.C. Gato**
IDMEC, Instituto Superior Técnico,
Universidade de Lisboa, Portugal

**R.P.F. Gomes**
IDMEC, Instituto Superior Técnico,
Universidade de Lisboa, Portugal

## ABSTRACT

The paper presents a performance analysis of a wave-energy converter designed for oceanographic applications to generate 300-500 W of electrical power on average. The prototype consists of a small draft cylindrical buoy connected to a submerged anti-heave plate by a hydraulic power take-off system and cable. Engineering details and design of the system are based on the results of a detailed time-domain hydrodynamic analysis of the system, discussed here. The performance of the prototype is assessed with respect to the submerged plate size/added-mass and the effectiveness of latching schemes. Additionally, results for the power extraction are statistically compared with measurements performed during field tests in Monterey Bay, California. During these tests performance measurements were logged by the buoy, and wave data was recorded by a measurement buoy positioned 1 km from the deployment site. This allows the comparison of actual performance to model predictions run for the sea state present during testing. In general, the results of the numerical model match fairly well with the data acquired in field testing. The proposed causal latching control schemes have been shown to be ineffective for this type of wave-energy converter.

## 1 Introduction

The Monterey Bay Aquarium Research Institute (MBARI) has been developing a wave-energy conversion buoy specifically for powering oceanographic instrumentation. The resulting device is a two-body point absorber in which a power take-off device connects a surface buoy and a submerged anti-heave plate (see figure 1). The relatively low average power level requirements (300-500 W) and small size make this system distinct from the larger wave-energy conversion devices currently being explored for utility power applications. Nevertheless, it is still important to develop as much power as possible from these systems with respect to their size and weight. The work presented here is the result of a collaboration between MBARI and IDMEC/IST (Instituto de Engenharia Mecânica/ Instituto Superior Técnico) intended to utilize the computational tools from IDMEC/IST to explore advanced control schemes (latching in particular) to increase the amount of power captured by the MBARI system.

The future holds many ambitious projects for oceanographic data-acquisition systems. At-sea charging stations for autonomous underwater vehicles (AUVs) and autonomous un-moored platforms for extended deployments are examples of such projects that are underway and that we will likely see come to fruition in the coming years. The development of energy harvesting techniques for these systems is important and we aim to advance those efforts.

For this application of wave-energy, the low sea-state performance is particularly important to maintain high average powers, i.e., it is not hard to meet the power goals in higher sea-states and the total energy capture quickly becomes limited by on-board energy storage limitations. For this reason the low sea-state performance is the biggest factor limiting the average power this system can make available to systems it hosts.

Up to the point of this work, the MBARI system had been deployed only with a linear damping scheme in which the power take-off machinery exerts a force that is proportional to the relative speed between the surface buoy and submerged plate. Latching control is a technique of phase control developed by Budal and Falnes [1] and consists of latching the device in a fixed position, during certain intervals of the wave cycle, to approximately bring into phase the body velocity and the excitation force on the body. The advantage of this technique is that it does not require that the system power electronics return energy to the hydraulic system and could therefore be directly applied to the existing system. The disadvantage of this approach is that it is suboptimal and has only been demonstrated to be effective in certain cases of two-body point absorbers.

Previous work at IDMEC/IST [2] had explored the utility of latching in larger two-body systems and shown that an increase in total power capture can be obtained when the inertia of the submerged element is significantly larger than the mass of the surface buoy. This work was undertaken to determine specifically if a similar method can be applied to this smaller scale system. The analysis presented here shows that at the small scale of this system, latching techniques are only efficient for inertia ratios (submerged element inertia to buoy mass) above 25:1, ratios that are impractically large for this system. This is in contrast to the findings of [2] that show an increase in power capture for inertia ratios of 5:1 for the larger systems. One possible explanation for this behavior is the impossibility of latching when the cable is slack, meaning that latching is only possible in the positive half-cycle of the diffraction force. The latching scheme was not implemented in the MBARI device but instead a test deployment was done with a plate larger than previously tested since the analysis suggested a strong relationship between that parameter and total energy capture.

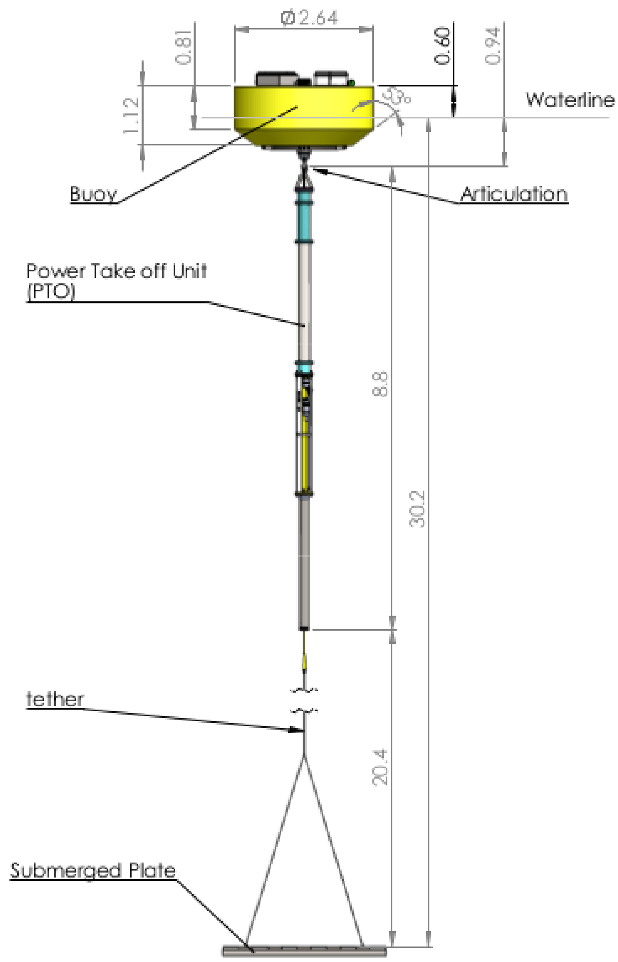


**FIGURE 1**: View of the MBARI's Wave-Power Buoy. Dimensions are in meters.

## 2 System description

The wave-energy conversion device considered here (see figure 1) consists of a cylindrical surface buoy connected to a submerged plate, 30 m below the surface, by an electro-hydraulic power take-off system.

The surface buoy is typical of oceanographic systems and houses batteries, system control and power electronics, and other instrumentation. The physical parameters of the surface buoy are:

- diameter: $D = 2.5\,\mathrm{m}$;
- water-plane area: $S = 4.9\,\mathrm{m}^2$;
- mass (with PTO system attached): $m_1 = 1520\,\mathrm{kg}$;
- displacement (with PTO system and plate attached): $2.29\,\mathrm{m}^3$.

The submerged plate is a welded steel frame with aluminum plates that can be arranged to provide different drag and added mass characteristics without significantly changing the submerged plate's mass. The system has been deployed with several configurations of the submerged plate, allowing performance sensitivity to various parameters to be evaluated. The drag coefficient and added mass values are obtained as estimates from both numerical analysis using CFD and WAMIT as well as full-scale lab tests. For extended deployments the submerged plate is anchored to the sea-floor with a chain-catenary mooring. It is not believed this mooring is a significant factor in the dynamics of the system because the mean tensions in the system vary little with changing sea, wind, and current conditions. That is, the mooring loads are small compared to the inertial and drag forces the submerged plate exerts on the surface buoy through the power take-off system. The physical properties of the submerged plate used in the field test presented here are:

- area: $A_p = 13.7\,\mathrm{m}^2$;
- mass: $m_3 = 970\,\mathrm{kg}$;
- added mass: $A_3^\infty = 10140\,\mathrm{kg}$;
- drag coefficient: $C_D = 1.9$.

The power-take-off device is the most complicated part of the system and consists of an electro-hydraulic device as a damping element and a pneumatic spring element arranged in parallel. The damping component is a hydraulic cylinder plumbed directly to a hydraulic motor (bent-axis piston type). The hydraulic motor is coupled directly without a gearbox to a permanent-magnet motor operating as a generator. There is no accumulator in the system and the generator and hydraulic motor stop and reverse direction with each oscillation of the power take-off ram. The small size and low inertia of the system allows this and while some oscillations are present due to the compressibility of the hydraulic oil reacting against the rotational inertia when the system is lightly loaded. These oscillations are heavily damped for all tested loads. The absence of an accumulator simplifies the system and eliminates a loss element, but does result in a wide range of voltage and power levels that the power electronics must convert to battery bus voltages. Presently this is accomplished by DC-DC converters in the system, with any excess power being shunted to a resistive load dump to maintain a load on the system at all times. This arrangement allows for simple electronic control of the load presented to the wave-energy converter. The mechanical-to-electrical efficiency of this power take-off device has been measured to be between 65 and 75 percent, depending on the condition of the seals and the care with which the long hydraulic rams are aligned. Like most hydraulic systems, efficiency is better at high damping levels (and subsequent high oil pressures). The numerical modeling below characterizes the system's ability to capture wave energy as a function of this damping force and it is seen to be fairly insensitive to this value, allowing the hydraulic system to operate at its most efficient point in almost all conditions. The hydraulic PTO system has the following characteristics:

- bore diameter 6.35 cm (2.5 in);
- rod diameter 3.81 cm (1.5 in);
- total stroke: 2 m;
- maximum damping force is approximately 20000 N (set by a pressure relief valve).

The spring element in the system consists of a second piston working against two volumes of compressible gas. The gas pressures and volumes are selected to create a nearly linear spring of appropriate spring constant which is not adjustable. The characteristics of this element are:

- Upper chamber
  - absolute pressure: 5.2 bar;
  - chamber volume: $0.036\,\mathrm{m}^3$.
- Lower chamber
  - absolute pressure: 8.7 bar;
  - chamber volume: $0.062\,\mathrm{m}^3$.

The control system on-board the buoy measures a range of parameters at 10Hz throughout the deployments. In addition to logging this data and transmitting it to shore in near real-time, the damping force exerted is controlled electronically as a function of piston speed (or any other parameter) at a rate of 10Hz. The following data is recorded:

- piston position;
- force between buoy and PTO system;
- pressure and temperature sensors to monitor spring gas conditions;
- pressure sensor to monitor sea pressure at top of the PTO (buoy draft);
- Six degree-of-freedom GPS aided inertial measurement unit to measure the buoy motions and location;
- generator voltage;

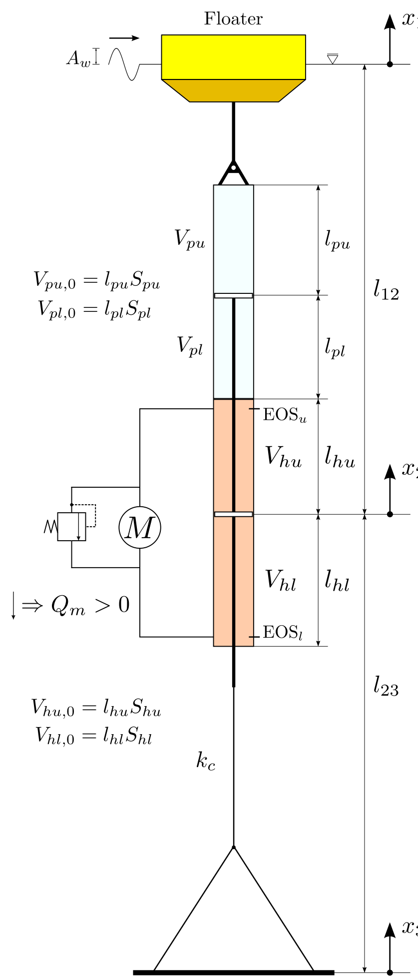


**FIGURE 2**: Conceptual model of the MBARI ocean's wave energy converter. $x_1$, $x_2$ and $x_3$ are local coordinate systems and the zero is at the equilibrium positions without waves.

- generator current;
- battery bus voltage and current.

## 3 Numerical modeling

The buoy and the plate are only allowed to move in heave and they are connected through the PTO system. The distance from the submerged plate to the free surface is assumed to be large enough for the excitation and radiation forces on the plate to be neglected. Furthermore, the hydrodynamic interaction between the floater and the submerged plate is neglected.

The numerical modeling is performed in the time domain and solves the equations of motion of four elements simultaneously: the buoy, the piston, the hydraulic motor/generator (rotational motion), and the submerged plate. The equations of motion for the system are written in terms of the vertical coordinates $x_i$ defining the position of body $i$ ($i = 1,2,3$), with $x_i = 0$ in the absence of waves and $x_i$ increasing upwards. The floater is denoted as 1, the piston as 2, and the submerged plate as 3. See figure 2.

### 3.1 The floater

The equation of motion for the floater is

$$(m_1 + A_1^\infty)\ddot{x}_1 = -\rho g S x_1 + F_{\text{ext}} - F_{\text{rad}} + F_{\text{gas}} + F_{\text{M}}, \qquad (1)$$

where a dot represents time derivative. Here, $g$ is the acceleration of gravity, $\rho$ is water density, $A_i^\infty = \lim_{\omega\to\infty} A_i(\omega)$, where $A_i(\omega)$ is the frequency dependent added mass coefficient for body $i$ and $F_{\text{ext}}$ is the excitation force modeled as in [2]. The radiation force $F_{\text{rad}}$ is computed in the time domain as

$$F_{\text{rad}} = \int_{-\infty}^{t} K_1(t-\tau)\dot{x}_1(\tau)\,d\tau. \qquad (2)$$

See [3] for further details.

The force acting on the piston is modeled assuming an isentropic compression/expansion ($pV^\gamma = p_0 V_0^\gamma$) resulting, after some manipulation, in

$$F_{\text{gas}} = F_{\text{pu0}}\left(1 - \frac{x_2 - x_1}{l_{\text{pu}}}\right)^{-\gamma} - F_{\text{pl0}}\left(1 + \frac{x_2 - x_1}{l_{\text{pl}}}\right)^{-\gamma}, \qquad (3)$$

where $F_{\text{pu0}} = p_{\text{pu0}}A_{\text{pu}}$ and $F_{\text{pl0}} = p_{\text{pl0}}A_{\text{pl}}$. As in Fig. 2, subscripts pu, pl refer to the pneumatic upper chamber and the pneumatic lower chamber, respectively. The subscript 0 denotes mid-stroke conditions.

Assuming oil as an incompressible fluid, the force on the hydraulic cylinder is given by

$$F_{\text{M}} = A_{\text{oil}}\Delta p_{\text{oil}}, \qquad (4)$$

where $A_{\text{oil}} = A_{\text{piston}} - A_{\text{bore}}$ is the wet piston area.

### 3.2 Hydraulic piston

The equation of motion for the piston is

$$m_2\ddot{x}_2 = -F_{\text{gas}} - F_{\text{M}} - F_{\text{mg},2} - F_{\text{cable}}. \qquad (5)$$

$F_{\text{mg},2} = m_2 g$ is the weight of the piston and rods. The tether force is given by

$$F_{\text{cable}} = k_c \max(x_2 - x_3, 0), \qquad (6)$$

where $k_c$ is the stiffness of the cable.

**TABLE 1**: MBARI's Wave-Power Buoy system characteristics used in the simulations

| Floater | | Power Take-off | | | | | | Hydraulics | | Generator |
|---|---|---|---|---|---|---|---|---|---|---|
| $D$ | $A_\infty^1$ | $p_{\text{pu}}$ | $l_{\text{pu}}$ | $S_{\text{pu}}$ | $p_{\text{pl}}$ | $l_{\text{pl}}$ | $S_{\text{pl}}$ | $A_{\text{oil}}$ | $D_m$ | $J_{\text{gen}}$ |
| [m] | [kg] | [bar] | [m] | [m$^2$] | [bar] | [m] | [m$^2$] | [m$^2$] | [m$^3$/rad] | [kg m$^2$] |
| 2.5 | 2805 | 8.690 | 2.868 | 0.0127 | 8.690 | 0.0127 | 0.0115 | $8.87\times10^{-4}$ | $0.77986\times10^{-6}$ | $1.13\times10^{-3}$ |

### 3.3 Submerged plate

The motion of the submerged plate is given by

$$(m_3 + A_3^\infty)\ddot{x}_3 = F_{\text{cable}} - F_{\text{mg},3} - F_{\text{drag}}, \tag{7}$$

where $F_{\text{mg},3} = m_3\, g$, $F_{\text{drag}} = \frac{1}{2}\rho\,\dot{x}_3|\dot{x}_3|A_p C_D$ and $A_p$ is the plate area. It should be noted that when the cable is slack, $F_{\text{cable}} = 0$, Eq. (7) is decoupled from Eqs. (1) and (5).

### 3.4 Hydraulic motor

The theoretical volume flow rate and torque of the motor are given by

$$Q_m = D_m\, \omega_m, \tag{8}$$

$$T_m = D_m\, \Delta p_{\text{oil}}, \tag{9}$$

where $D_m$ is the volumetric displacement of the motor and $\omega_m$ is the rotational speed in radians per unit time. The theoretical volume flow rate of the motor is related to the cylinder motion (actual volume flow rate) through

$$D_m\, \omega_m = A_{\text{oil}}\, (\dot{x}_2 - \dot{x}_1)\,. \tag{10}$$

The generator motion is modeled using

$$J\dot{\omega}_m = T_m - T_{\text{gen}}, \tag{11}$$

which yields

$$\frac{JA_{\text{oil}}}{D_m}\,(\ddot{x}_2 - \ddot{x}_1) = D_m \Delta p_{\text{oil}} - T_{\text{gen}}, \tag{12}$$

where the generator torque is given by the control relationship

$$T_{\text{gen}} = C_{\text{gen}}\,(\dot{x}_2 - \dot{x}_1)\,. \tag{13}$$

The constant $C_{\text{gen}}$ is used to control the power extracted by the electrical generator.

Eq. (12) can be written in a form which allows a direct substitution of $F_{\text{M}}$ in Eqs.(1) and (5)

$$F_{\text{M}} = m_J\,\ddot{x}_2 - m_J\,\ddot{x}_1 + F_{\text{gen}}, \tag{14}$$

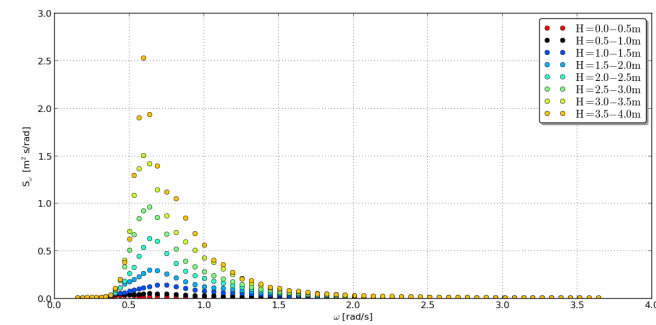


**FIGURE 3**: May sea spectra.

where $m_J = JA_{\text{oil}}^2 D_m^{-2}$ and $F_{\text{gen}} = A_{\text{oil}} T_{\text{gen}} D_m^{-1}$.

### 3.5 Numerical solution

The numerical model comprises the system of equations (1), (5) and (7). Since latching implies a non-linear process, the equations of motion must be solved in the time-domain. In this paper, we use the high-order numerical method proposed in [2] for the solution of the system of equations. This approach is based on a continuous polynomial representation of the solution whose coefficients are computed using a continuous least-squares approximation. A sixth-order polynomial was used for the computation of the bodies' positions. The convolution integral is calculated using the continuous polynomial approximation of the velocity as computed by the least-squares method. This constitutes an important advantage of the proposed method in comparison to the usual high-order Runge-Kutta methods, in which the convolution integral is computed with the trapezoidal rule, limiting the overall accuracy of the solution to second-order. In the present approach, the convolution integral is computed using a Gauss-Legendre quadrature rule which results in a product of a matrix by a vector of instantaneous velocities.

The code has been successfully parallelized using the OpenMPI library to largely reduce the computational time. For the computations, each spectrum is assigned to one processor. The computations were performed at the IST cluster.

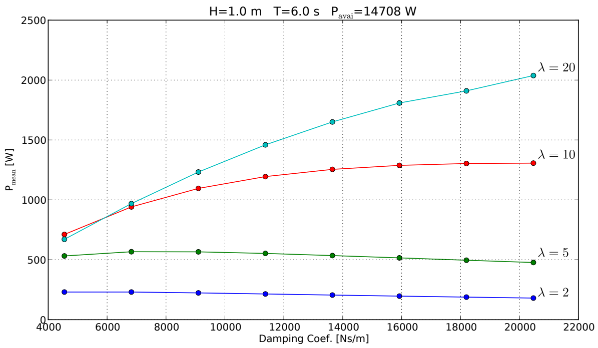


(a) $T = 6\,\mathrm{s}$

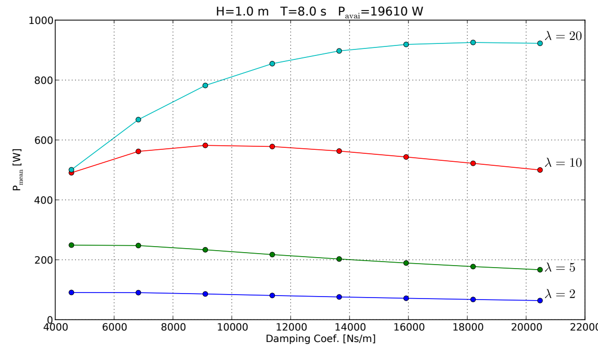


(b) $T = 8\,\mathrm{s}$

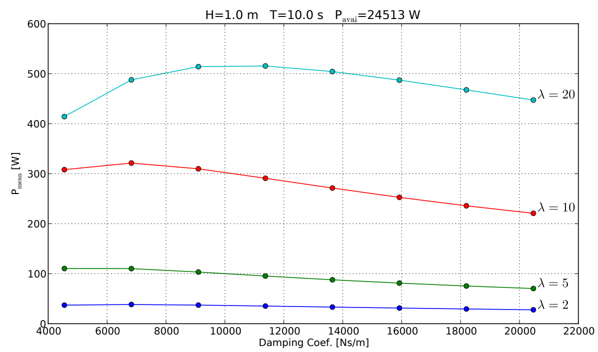


(c) $T = 10\,\mathrm{s}$

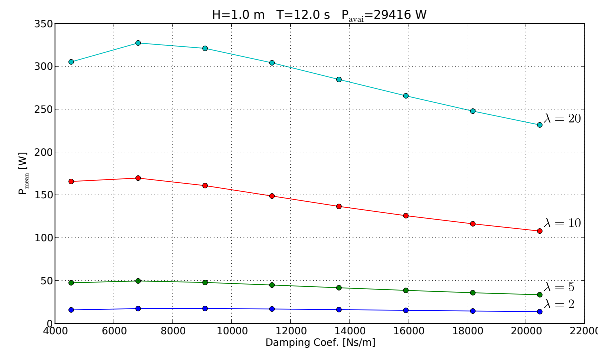


(d) $T = 12\,\mathrm{s}$

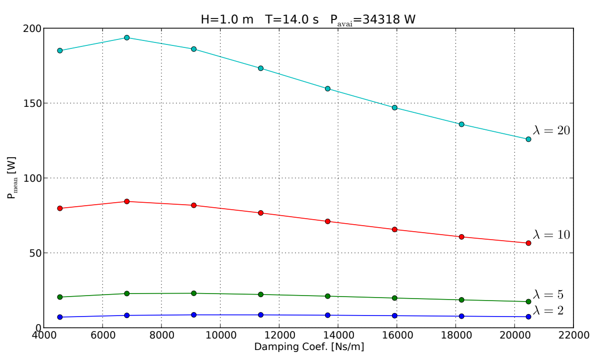


(e) $T = 14\,\mathrm{s}$

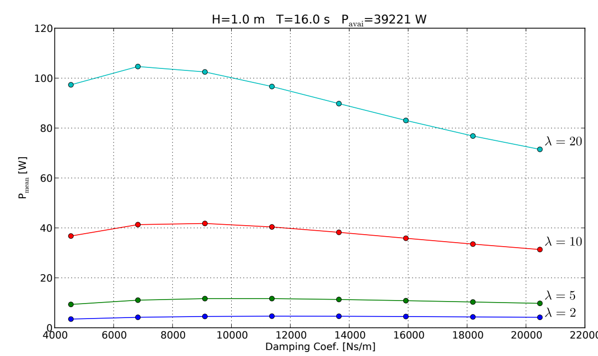


(f) $T = 16\,\mathrm{s}$

**FIGURE 4**: Mean power conversion, $P_{\mathrm{mean}}$, as function of $\lambda$ and $C_{\mathrm{sys}}$, for regular waves with $H = 1.0\,\mathrm{m}$ and different periods.

## 4 Numerical and field test results

Two types of numerical studies have been performed, the first to evaluate the system's performance with various values of linear damping coefficient and submerged plate added mass. The second explores the effects of latching control schemes for this system at various values of submerged plate added mass. The submerged plate added mass is found to be an important parameter in both cases. Additionally, results from field tests performed in May 2013 in Monterey Bay are compared to the numerical predictions.

For the system characteristics shown in table 1, the extracted power from the wave energy converter was studied as a function of two main parameters: the system damping coefficient, defined as

$$C_{\mathrm{sys}} = \frac{C_{\mathrm{gen}} A_{\mathrm{oil}}}{D_m}, \tag{15}$$

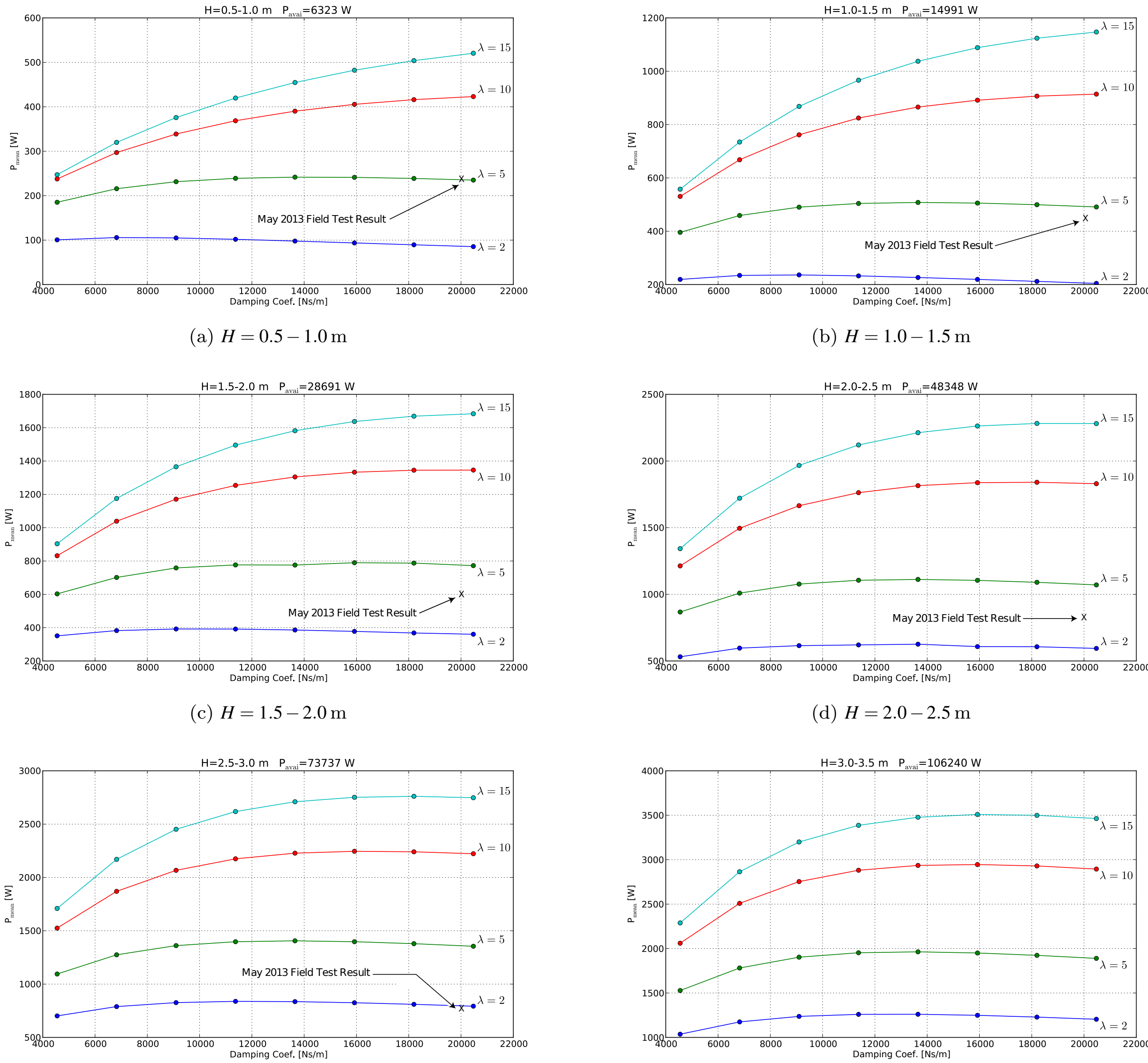


(a) $H = 0.5 - 1.0\,\mathrm{m}$ (b) $H = 1.0 - 1.5\,\mathrm{m}$

(c) $H = 1.5 - 2.0\,\mathrm{m}$ (d) $H = 2.0 - 2.5\,\mathrm{m}$

(e) $H = 2.5 - 3.0\,\mathrm{m}$ (f) $H = 3.0 - 3.5\,\mathrm{m}$

**FIGURE 5**: Mean power conversion, $P_{\mathrm{mean}}$, as function of $\lambda$ and $C_{\mathrm{sys}}$, for each of the May spectra. There is no field test result for (f) because waves in this height range did not occur during the deployment period.

and the dimensionless plate added mass

$$\lambda = \frac{m_3 + A_3^{\infty}}{m_1}. \tag{16}$$

For regular waves in deep water, the time-averaged energy flux per unit of wave crest length is given by

$$P_{\mathrm{avai}} = \frac{\rho g^2 H^2}{16\omega}. \tag{17}$$

Under linear water wave theory, the resulting diffraction force for a spectrum is obtained as a superposition of $N$

```
switch (latch_stage) {
    case 0:
      // If oil pressure crosses zero falling then initiate timers
      //
      if( dp_oil(0) > dp_oil(Delta_tau) and dp_oil(Delta_tau) < 0.0 ) {
        UnlatchTimer.Trigger(t, sys.t_unl);
        LatchTimer.Trigger(t, sys.t_lat);
        LatchStage = 1;
      }
      break;
    case 1:
      // If the unlatched timer has elapsed then the system
      // is unlatched
      if( UnlatchTimer.Elapsed(t) ) {
        LatchStage = 2;
        IsLatched = false;
      }
      break;
    case 2:
      // If relative velocity is zero and the secondary timer has
      // elapsed then
      // latch the system.
      //
      // The secondary timer is used to avoid spurious
      // latching orders due to oscillations in the cable.
      //
      if( dx_r(0) * dx_r(n_tau - 1) <= 0.0 and dx_r(n_tau - 1) < 0.0
          and LatchTimer.Elapsed(t) ) {
        LatchStage = 0;
        IsLatched = true;
      }
  }
```

**FIGURE 6**: Stages of the latching algorithm written in C++. The code is executed once at the end of each time step.

frequency components

$$F_{\text{ext}}(t) = \sum_{j=1}^{N} \Gamma(\omega_j) A_{\omega_j} \cos(\omega_j t + \phi_j), \tag{18}$$

with

$$A_{\omega_j} = \sqrt{2\Delta\omega_j S_{\omega,i}}, \tag{19}$$

$$\Delta\omega_j = (1 + \varpi_j)\Delta\omega, \tag{20}$$

$$\omega_j = \omega_{j-1} + 0.5\left(\Delta\omega_j + \Delta\omega_{j-1}\right), \quad j = 2, \ldots, N, \tag{21}$$

where $\Gamma(\omega_j)$ is the excitation force coefficient computed using WAMIT, $\phi_i$ is a phase constant equal to a random number between 0 and $2\pi$, $\varpi_j$ is a random number between 0 and 0.2 and $S_{\omega,i}$ is the frequency spectral density function. The inclusion of the perturbation $\varpi_j$ has been shown to avoid repeating patterns appearing in the time records constructed from the superposition of frequency components [2]. In deep water, the time-averaged energy flux per unit of wave crest length for a specific spectrum is given by the sum of the power of each sinusoidal wave

$$P_{\text{avai}} = \frac{\rho g^2}{4} \sum_{j=1}^{N} \frac{A_{\omega_j}^2}{\omega_i}. \tag{22}$$

### 4.1 Linear damping behaviors

Figure 4 shows the numerically predicted power across a range of damping coefficients, inertia ratios ($\lambda$), and wave periods. The mean power conversion under regular waves was computed for several wave periods $T = 6, 8, 10, 12, 14$ and 16 s and a wave height of $H = 1.0$ m. The total simulation time considered was 1200 s with a time step of $\Delta t = 0.1$ s.

The reported average values of power represent mechanical power and don't include inefficiencies in the mechanical to electrical conversion process. These basic results illustrate a strong dependence on the submerged plate added-mass, and a weak dependence on the system damping coefficient. Even at the smaller inertia ratios, the predicted performance degrades only slightly for high values of the damping coefficient. This is important because as described above the hydraulic power take-off device is most efficient at high loadings.

To estimate the power capture capabilities of the system in irregular waves, the numerical model was run with a range of spectra that represent the expected conditions at the test deployment site. Figure 3 shows the characteristic spectra used. These were derived from 5 years of measured data at the deployment site. All the calculations were performed assuming $N = 300$, $\omega_1 = 0.63$ rad/s and $\Delta\omega = 2.46/(N-1)$ rad/s, see Eqs. (18)-(21). Each measured spectrum during the 5 years of May measurements represents the conditions during a half-hour period, and each has an associated significant wave height. All the measured spectra for each range of significant wave-heights were averaged to create a representative spectrum. Figure 5 shows the model predictions and includes a data point that shows the actual average power production measured during the at-sea tests performed in May 2013 with a non-dimensional plate added mass of $\lambda = 5$. Because the at-sea system logs electrical power, the data points shown on the plots are the measured electrical power divided by the power-take-off device efficiency factor that was measured in the lab, allowing comparison between the numerical and measured results. The agreement is quite good in the milder sea-states but degrades in larger waves, possibly due to viscous losses and/or a discrepancy between the sea states actually present during the tests and the representative spectra used to drive the numerical model. A more accurate comparison would re-run the model for each and every sea-state encountered during the test and compare the predicted versus measured power production for each half-hour spectra integration pe-

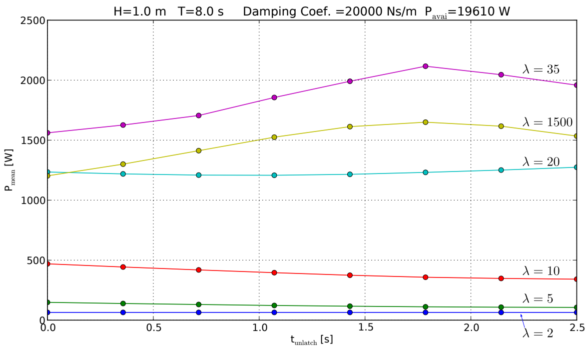


(a) $T = 8\,\mathrm{s}$ and $C_{\mathrm{sys}} = 20000\,\mathrm{Ns/m}$

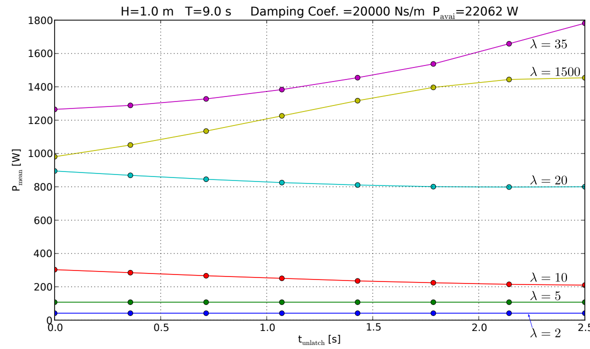


(b) $T = 9\,\mathrm{s}$ and $C_{\mathrm{sys}} = 20000\,\mathrm{Ns/m}$

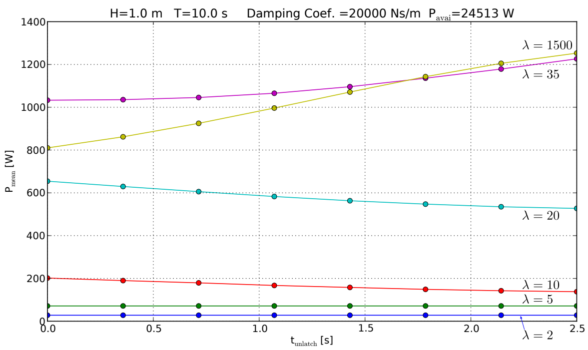


(c) $T = 10\,\mathrm{s}$ and $C_{\mathrm{sys}} = 20000\,\mathrm{Ns/m}$

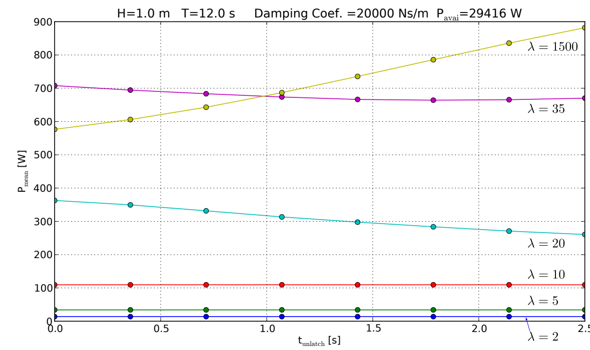


(d) $T = 12\,\mathrm{s}$ and $C_{\mathrm{sys}} = 20000\,\mathrm{Ns/m}$

**FIGURE 7**: Mean power conversion, $P_{\mathrm{mean}}$, using latching control as function of $\lambda$ and unlatched time interval, $t_{\mathrm{unlatch}}$, for regular waves with $H = 1.0\,\mathrm{m}$ and different periods. $t_{\mathrm{unlatch}} = 0$ corresponds to linear damping with no latching effects.

riod. This has not been done at this point but the efficiency of the numerical scheme presented above makes this possible.

## 4.2 Latching control behaviors

The causal (sub-optimal) latching algorithm used is shown in Fig. 6 and it is based on [2]. The algorithm detects when the oil pressure crosses zero and then starts a timer that waits for a time period of $t_{\mathrm{unlatch}}$ to unlatch the system. Then, when the relative velocity between the floater and the piston is zero, the system is latched again. To avoid spurious latching orders due to cable oscillations a secondary timer is triggered which disables latching orders immediately after unlatching.

Utilizing the numerical tools described above and the latching algorithm described, numerical results have been computed for regular waves and the mean power conversion results using phase control by latching are presented in Fig. 7 for regular waves with periods of $T = 8, 9, 10$ and $12\,\mathrm{s}$. The total simulation time was $1200\,\mathrm{s}$ with a time step of $\Delta t = 0.005\,\mathrm{s}$.

Results for the system with latching are shown in Fig. 7 and demonstrate this scheme to be ineffective for this wave-energy converter, i.e. the latching algorithm tends to lower the average extracted power as the submerged plate movement. Only for very high submerged plate added mass (very high $\lambda$) would latching start to be successful and these ratios are beyond what is practical to field. The results shown are computed for a damping coefficient of $C_{\mathrm{sys}} = 20000\,\mathrm{Ns/m}$ and similar behaviors were seen for other values of damping coefficient.

## 4.3 Field results

Figure 8 shows hourly averages of the power captured for five different test deployments at Monterey Bay, California, in different system configurations and sea conditions. The May 2013 deployment had the largest submerged plate added mass and subsequently performed the best, especially at lower sea states. The lack of an increase in the measured results at higher sea states in figure 8 is likely due to the

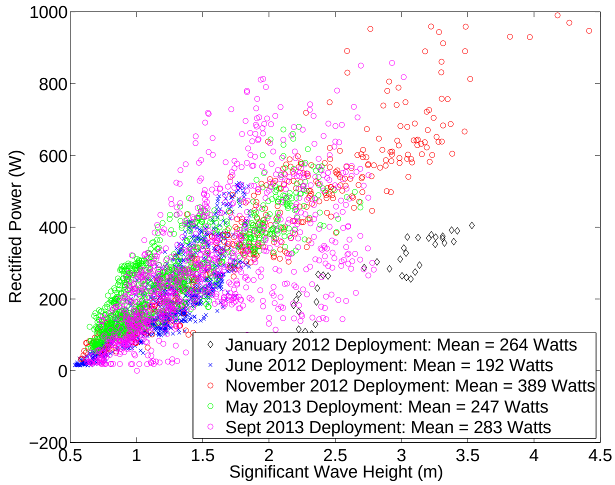


**FIGURE 8**: Hourly electrical power averages throughout five test deployments.

fact that the system sheds peak pressures in the hydraulic system through a pressure relief valve.

## 5 Conclusions

It is evident that the mean power extracted increases substantially with the $\lambda$ coefficient, i.e., with the submerged anti-heave plate added mass. For wave periods between 8 s and 16 s, the mean power curves present an optimal damping value, $C_{\mathrm{sys}}$, although the total energy capture is not very sensitive to this parameter. The same analysis was performed for the spectra that represent the wave climate of May at the test site. As in regular wave results, the mean power extracted increases with plate added mass. For the various sea states and $\lambda$ curves, $P_{\mathrm{mean}}$ exhibits a "plateau-like" behavior when increasing the damping coefficient, i.e. after a given threshold $P_{\mathrm{mean}}$ is weakly dependent of the damping coefficient.

Due to the impossibility of measuring the wave conditions in real-time, a causal (sub-optimal) phase control by latching was proposed, with the objective of increasing the wave power absorption. The numerical computations show that the applied latching control did not improve power extraction due to the following reasons:

- During the latched period, the floater/submerged plate pair cannot be kept fixed, unlike the case of a single body reacting against a fixed reference, thus reducing latching performance. In this case, the two bodies move together with the combined two-body dynamics.
- A large increase in the second body inertia (plate mass plus added mass) reduces the motion of the submerged plate. However, in this case, latching is only possible while the cable is subjected to tensile forces. So, phase control can only be applied when the buoy has positive velocity, tipically half wave cycle.
- In order to limit brake forces on the system, the braking should occur approximately when the relative velocity between floater and the anti-heave plate is zero ($\dot{x}_1 - \dot{x}_2 = 0$).

Although the numerical simulations of latching did not lead to an increase in power capture in the prototype system, this work highlighted the importance of the submerged plate inertia in the energy extraction.

For small wave-energy harvesting systems of this type, the most expedient way to increase the power capture is to increase the size, mass, and drag of the submerged element of the system and utilize simple linear-damping power take-off devices. The limits to this approach are the large peak loads and the implications for storm survivability. The natural development path is towards compliant sub-surface heave plates that can exert large inertial and drag forces in moderate sea states but that can shed power in larger sea states.

The successful deployment of MBARI's wave power buoy in May 2013 at Monterey Bay, California, confirmed the numerical simulations. The system had a larger submerged plate added mass and performed better than previous deployments, especially at lower sea states.

## REFERENCES


[1] Falnes, J., and Budal, K., 1978. "Wave power conversion by point absorbers". *Norwegian Maritime Research,* ***6***(4), pp. 2–11.

[2] Henriques, J. C. C., Lopes, M. F. P., Gomes, R. P. F., Gato, L. M. C., and Falcão, A. F. O., 2012. "On the annual wave energy absorption by two-body heaving WECs with latching control". *Renewable Energy,* ***45***, pp. 31–40.

[3] Henriques, J. C. C., Falcão, A. F. O., Gomes, R. P. F., and Gato, L. M. C., 2013. "Air turbine and primary converter matching in spar-buoy oscillating water column wave energy device". In Proceedings of the 32nd International Conference on Ocean, Offshore and Arctic Engineering.